Photoconductivity of GeSn thin films with up to 15% Sn content

Serhiy Kondratenko,[1,*] Oleksandr Datsenko,[1] Andrian V. Kuchuk,[2] Fernando M. de Oliveira,[2] Danylo Babich,[1] Peter M. Lytvyn,[3] Morgan E. Ware,[2,4] Volodymyr Lysenko,[3] Shui-Qing Yu,[4] Yuriy I. Mazur,[2,†] and Gregory J. Salamo[2]

[1]*Taras Shevchenko National University of Kyiv, 64 Volodymyrs'ka Street, 01601 Kyiv, Ukraine*
[2]*Institute of Nano Science and Engineering, University of Arkansas, Fayetteville, Arkansas 72701, USA*
[3]*V. E. Lashkaryov Institute of Semiconductors Physics, NAS of Ukraine, 41 Prospekt Nauki Avenue, 03028 Kyiv, Ukraine*
[4]*Department of Electrical Engineering, University of Arkansas, Fayetteville 72701, USA*

(Received 14 February 2023; revised 3 June 2023; accepted 13 June 2023; published 14 July 2023)

We have used temperature-dependent photoconductivity (PC) with different excitation wavelengths and intensities to study the photoexcited charge-carrier transport within GeSn/Ge/Si heterostructures. The evolution of the PC spectra with temperature was analyzed between 10 and 200 K. These strained GeSn films were grown with high enough Sn content such that the band gaps were direct. As such, the relationships between the band gaps and the temperature were determined using photoconductivity spectroscopy. As a result, an anomalous, linear blueshift of the PC spectral edge was found with increasing temperature. This was attributed to the variation of the GeSn band gap within the film, due to variations in strain and the increased contribution to PC from the region of highest Sn content. The change in photocurrent with excitation intensity and temperature demonstrates that conduction occurs predominantly through the GeSn and Ge layers under low optical pumping and through the Si substrate under high optical pumping. A phenomenological model of photoconductivity in GeSn as it depends on strain was proposed. This detailed understanding of the transport of photoexcited carriers along the GeSn layers is critical for developing GeSn/Ge-based optoelectronic devices.

DOI: 10.1103/PhysRevMaterials.7.074604

I. INTRODUCTION

The group-IV semiconductors Ge and Si have been the most widely studied materials since the emergence of electronics [1,2]. However, naturally occurring Ge and Si are both indirect-band-gap semiconductors. This has not slowed the march of Si-based devices towards smaller sizes and higher densities. The fabrication and operation of optical devices, however, is not favorable. With the addition of Sn this material system can form alloys with direct band gaps. This has been demonstrated with alloys of GeSn by increasing the Sn content to over 6%–10% [3,4]. As a result, studies of direct-band-gap GeSn alloys, which have processing requirements similar to Si, have recently opened a new opportunity to integrate photodetectors and light emitters along with other electronics directly on Si wafers. There has subsequently been significant progress in developing electrically and optically pumped lasers operating in the near-infrared range using this material [5,6]. Furthermore, the high absorption coefficient ($\alpha > 10^4$ cm^{-1}) along with the tunable band gap and lattice constant resulting from varying the GeSn composition are attractive for designing photodetectors [7,8] and multijunction solar cells. In addition, its high carrier mobilities are potentially attractive for high-speed transistors and optoelectronics [9,10]. However, these high-performance optoelectronic devices generally require a high Sn content to achieve a direct band gap. The indirect-to-direct band gap transition occurs at around 6% for relaxed alloys, while compressive strain shifts the crossover point towards higher concentrations of Sn. The strain relaxation, which promotes indirect-to-direct crossover at lower Sn contents, is accompanied by various imperfections of the crystal structure both in the bulk of the films and in the vicinity of their interfaces.

The design of high-speed IR photodetectors and light-emitting devices requires considerable attention to the nonequilibrium charge transport in the GeSn alloys. The photogeneration and recombination, in turn, are expected to depend on the crystalline quality and the presence or not of deep level defects. In GeSn alloys with a high Sn content grown on Ge or Si substrates, such defects arise due to growth challenges originating from extremely low equilibrium solubility of α-Sn in Ge [11], as well as the significant lattice mismatch between Ge (6.489 Å) and α-Sn (5.646 Å) of about 15%. Consequently, low temperatures are required for GeSn epitaxial growth to prevent dislocations, and point defects [12,13], as well as phase separation, which results in the precipitation of Sn in the bulk and the formation of Sn-rich droplets on the surface [14]. On the other hand, achieving high ($> 10\%$) Sn content at low temperatures leads to the relaxation of compressive strain. This results in the generation of threading dislocations, the formation of localized or extended amorphous inclusions, and the roughening of the surface [15]. These imperfections will largely determine the performance of optoelectronic devices by acting as nonradiative recombination centers. Therefore, studying photoconductivity (PC) can help to determine the influence of deep defect states on

*kondratenko@knu.ua
†yumazur@uark.edu

carrier lifetimes while also improving the understanding of their optical properties and band structure as functions of the Sn concentration. For example, previous studies showed that GeSn alloys are good photoconductors with a fundamental absorption edge shifted to the IR range below the edge of bulk Ge [16,17].

In our previous work [18], investigations have focused on the impact of deep defect levels on photoexcited carrier dynamics in GeSn thin films. In particular, the coinfluence of the band-to-band recombination and Shockley-Read-Hall (SRH) recombination was assumed to describe the temperature dependence of the carrier lifetime. The dislocation-related photoluminescence was dominant in the low Sn content indirect alloys and was responsible for the redshift of the PL bands relative to the absorption edge. A similar broad PL peak at 0.57 eV was observed in Ref. [19]. As Sn content increases, we expect various defects to be generated due to increased strain. Moreover, a smaller difference between the indirect and direct band gaps leads to a higher probability of band-to-band recombination and, therefore, higher concurrence with nonradiative paths for recombination.

In this paper, the results of temperature-dependent photoconductivity (PC) at different excitation wavelengths and intensities were applied to study the photoexcited charge-carrier dynamics as well as the in-plane transport in GeSn/Ge/Si heterostructures with high Sn content grown by chemical vaper deposition. By comparing the samples with various thicknesses and strains, we have clarified the photoconductivity mechanisms focusing on the impact of the vertical and in-plane variations of both the Sn content and the strain on the IR photoresponse of Sn-rich GeSn alloys. We have also analyzed the evolution of the PC spectra with temperature and have shown that the transport paths of photoexcited charge carriers occur mainly through the Ge buffer at high temperatures, while the GeSn film contributes more as the temperature decreases. Moreover, a GeSn-related IR photoresponse of the GeSn/Ge/Si heterostructures was found to be strongly dependent on variation of the band gap energies.

II. EXPERIMENT

The GeSn/Ge/Si heterostructures were grown using an industry-standard ASM EpsilonR 2000 Plus reduced pressure chemical vapor deposition (CVD) system with $SnCl_4$ and GeH_4 as Sn and Ge precursors, respectively. Boron-doped Si (100) with an acceptor concentration of 10^{15} cm^{-3} was used as a substrate for the growth of a 700-nm-thick Ge buffer followed by the GeSn thin films. The details of the GeSn growth by CVD including the $SnCl_4/GeH_4$ flow ratio [20–22] and control of the composition and strain [17] have been published elsewhere. Depending on the required Sn content, the growth temperature varied between 290 °C and 450 °C. As a result, a set of samples with Sn content of about 12% and thicknesses of 45 nm (sample S45), 100 nm (sample S100), 150 nm (sample S150), and 200 nm (sample S200) were grown at the same conditions to highlight the impact of strain relief on photoconductivity.

The x-ray diffraction (XRD) measurements were performed using a Panalytical X'Pert Pro MRD diffractometer equipped with a 1.6 kW x-ray tube (vertical line focus)

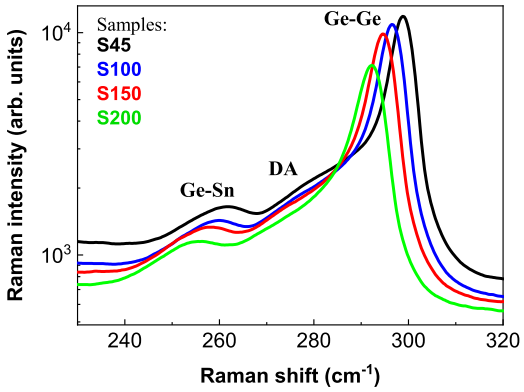

FIG. 1. The Raman spectra for samples of different thicknesses.

with Cu $K\alpha_1$ radiation ($\lambda = 1.540\,598$ Å), a symmetric $4 \times$ Ge(220) monochrometer, and a channel-cut Ge(220) analyzer.

Micro-Raman spectra were recorded at room temperature using a computer-controlled Raman spectrometer, LabRam HR-800 Horiba Jobin-Yvon, equipped with a thermoelectrically cooled CCD detector. For excitation, a 532 nm laser was focused on the GeSn surface into a ~ 1 μm diameter spot through an Olympus $100\times$ objective with a numerical aperture of 0.9. Micro-Raman spectra were measured in backscattering geometry from the (001) surface.

Two rectangular Ohmic In contacts, separated by 5 mm, with dimensions of 4×1 mm were annealed at 170 °C for photoconductivity measurements. The $J-V$ characteristics were linear in the range from –1 to +1 V at temperatures between 10 and 290 K, ensuring no rectifying impact on the PC signal. Photoconductivity measurements were performed under vacuum in a closed-cycle helium cryostat 331S by Advance Research System at temperatures from 10 to 290 K under a dc bias voltage of 100 mV. The photocurrent was excited using monochromatic light chopped at 120 Hz and was detected with a Stanford Research Systems SR860 lock-in amplifier with a SR570 low-noise current preamplifier. Spectral dependences were normalized to a constant number of photons using a nonselective pyroelectric detector.

A standard off-axis configuration was used to perform temperature-dependent photoluminescence (PL) measurements between 10 and 300 K. A continuous wave laser with a wavelength of 532 nm was used as the excitation source. The laser beam power was fixed at 500 mW and was focused to a 500 μm spot. The PL emission in the wavelengths range of 1400–2800 nm was detected by a spectrometer with a PbS detector.

III. RESULTS

A. Raman scattering and x-ray diffraction

Figure 1 shows the Raman spectra for samples of different thicknesses. Here, the peak from the Ge-Sn and the double peak related to the Ge-Ge mode in the film and the Ge-Ge mode in the buffer can be seen. A broad feature connecting the two peaks is also labeled as the disorder-activated (DA) mode. An exponentially modified Gaussian (EMG) function [23] was used for fitting the Ge-Ge peak that allows deriving two parameters: peak position (ω) and asymmetry (t). The

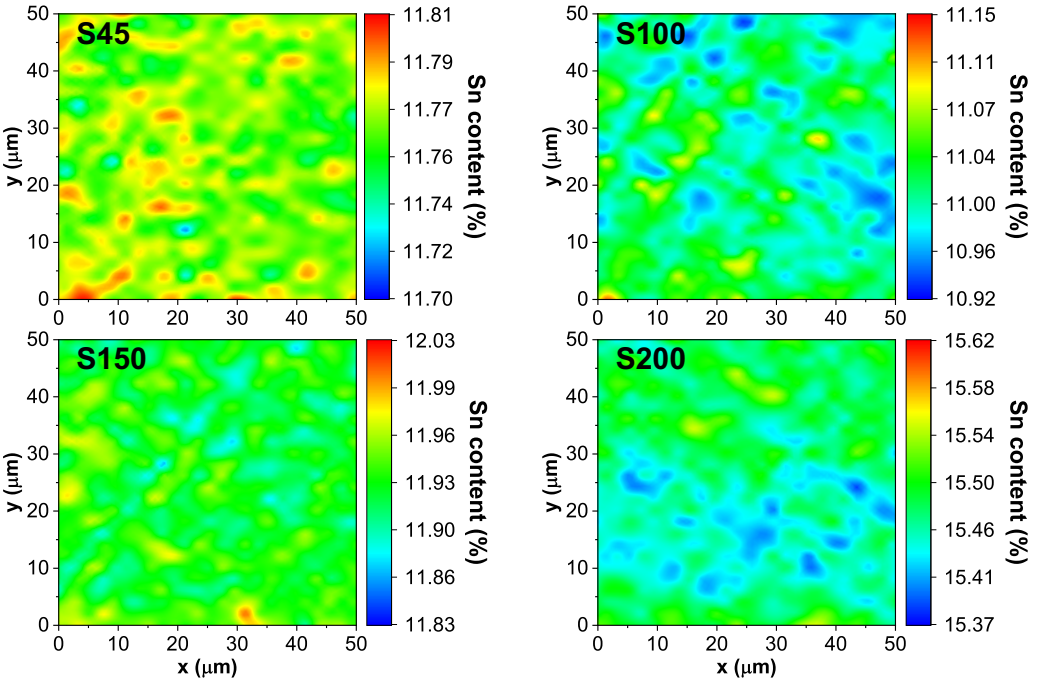

FIG. 2. The maps for Sn content for the samples of different thicknesses derived from the measured Raman spectra using Eqs. (1) and (2).

extracted measured peak position and asymmetry values were used to determine the Sn content (x) and strain value (ε_x) of the GeSn layer by solving the following equations [24,25],

$$\omega = \omega_0 + a_\omega x + b_\omega \varepsilon_x, \tag{1}$$

$$t = t_0 + a_t x + b_t \varepsilon_x, \tag{2}$$

where $\omega_0 = 300.4 \pm 0.9\ \mathrm{cm}^{-1}$, $t_0 = 1 \pm 0.1\ \mathrm{cm}^{-1}$, $a_\omega = -84 \pm 8\ \mathrm{cm}^{-1}$, $a_t = 6 \pm 1\ \mathrm{cm}^{-1}$, $b_\omega = -491 \pm 52\ \mathrm{cm}^{-1}$, and $b_t = -5 \pm 7\ \mathrm{cm}^{-1}$ are the fitting parameters for the Ge-Ge mode [26].

Figure 2 shows the derived maps for Sn content illustrating the gradual variations with a standard deviation in the range 0.014–0.037. A crosshatch pattern, which is common in atomic force microscopy (AFM) topography maps, becomes obvious along the perpendicular ⟨110⟩ directions for the thicker samples, S150 and S200. As a confirmation, AFM images shown in Figs. 3(a)–3(d), do indeed reveal crosshatch patterns oriented in the same direction as detected for the Sn content, although with a smaller periodicity ranging from ∼ 400 to ∼ 700 nm. This is due to the periodic strain fields induced by the presence of a regular array of misfit dislocations at the GeSn/Ge interface [27]. Variations of strain have also been observed in the ε_x maps derived from the Raman measurements (see Supplemental Material [28], Figs. 1S–4S). The histograms for Sn content and ε_x were fit by Gaussian functions and tend to increase distribution width with layer thickness [see Fig. 3(e)].

Reciprocal space maps (RSMs), measured around the asymmetric Ge(–2–24) reflection are shown in Figs. 4(a) and 4(b). Using these, the strain and Sn content were calculated using the approach described in detail in Ref. [29]. The sample parameters derived from XRD data are presented in Table I. A spontaneous change in composition is seen to occur

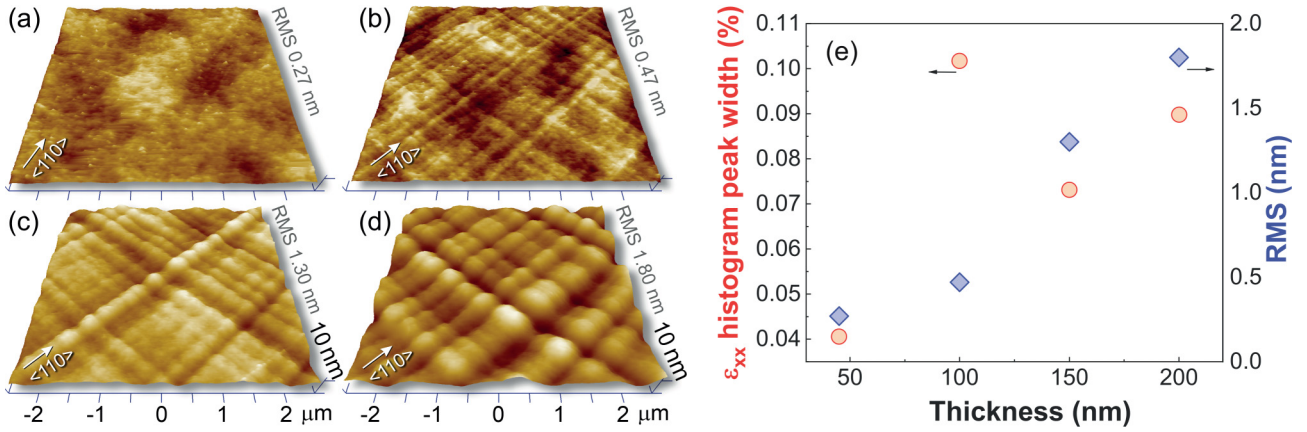

FIG. 3. (a–d) AFM images of the surface of GeSn layers of different thicknesses, (e) the surface rms roughness, and ε_x histogram peak width on the layer thickness.

TABLE I. Sn content and strain derived from Raman spectroscopy (RS) and XRD measurements.

Sample	Sn content from XRD (%)	Strain from XRD	Sn content from RS (%)	Strain from RS	Thickness (nm)
S45	11.77	−1.49	11.77	−2.04	45
S100	11.6	−1.36	11.01	−1.55	100
S150	13.7	−0.93	11.92	−1.18	150
	11.9	−0.67			
S200	14.9	−0.81	15.46	−1.52	200
	11.8	−0.36			

with increasing film thickness > 100 nm. Double contribution to RSMs from $Ge_{1-x}Sn_x$ were observed for samples S150 [Fig. 4(c), film thickness ∼ 150 nm] and S200 [Fig. 4(d), 200 nm], indicating the formation of two sublayers with different Sn content (x) and strain values (ε_x). In particular, sample S150 consisted of a bottom $Ge_{88.1}Sn_{11.9}$ and a top $Ge_{86.3}Sn_{13.7}$ layer, with ∼ 0.67% and ∼ 0.93% compressive strain, respectively. Sample S200 was found to consist of a bottom $Ge_{88.}Sn_{11.8}$ and a top $Ge_{85.1}Sn_{14.9}$ layer, with ∼ 0.36% and ∼ 0.81% compressive strain, respectively. As can be seen in Table I, the bottom layers had nearly the same Sn content and strain for all of the studied samples, because the growth conditions were kept the same between samples. Interestingly, the Raman measurements, as also summarized in Table I, generally agree with the composition and strain for samples S45, S100, and S150 (bottom layer), but with sample S200, the Raman correlates with the top layer composition and strain. This can be understood as being due to the penetration depth of the 532 nm laser used for excitation in the Raman spectral measurements. Since it only penetrates a few tens of nanometers, for S200, it only probes the top layer, and for S150 it probes both, but is obviously dominated by the bottom.

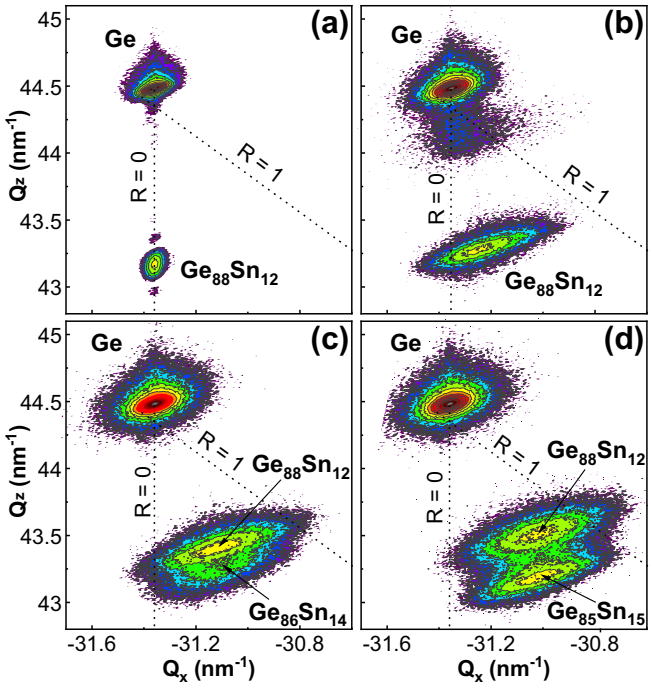

FIG. 4. Reciprocal space maps (RSMs) measured around asymmetrical Ge(–2–24) reflection.

B. Spectral dependence of photoconductivity and photoluminescence

Figure 5(a) shows the lateral PC spectra of the GeSn/Ge/Si heterostructures measured at 10 K from 0.4 to 2.0 eV. All the spectra contain the contributions originating from light absorption by GeSn films, Ge buffer, and the Si substrate. In the low-energy region below the absorption edge of Ge at 0.73 eV, the electron-hole pairs photoexcited in the GeSn thin film dominate the PC. Since photocurrent above the band edge is directly proportional to the absorption coefficient and its spectral dependence slowly deviates from the absorption spectrum, analyzing the spectral dependencies enables derivation of the band gap of GeSn alloys. In this connection, the photocurrent spectra in the near-band-gap region were presented in the Tauc coordinates $(I_{PC}h\nu)^2$ vs excitation energy $h\nu$, showing linear sections that allow determining the direct band gaps of the GeSn alloys accurately [Fig. 5(b)]. We have found that the band gap of the GeSn alloys decreases monotonously from 580 meV for the strained GeSn alloy (S45) to 490 meV for the thicker film (S200). This shift illustrates the well-known [30,31] impact of strain on the position of the absorption edge of GeSn thin films when a relaxation decreases the band gap. Besides the shift to lower energies, the photocurrent amplitude is unexpectedly lower for the thicker samples, S150 (150 nm) and S200 (200 nm), where a Sn-rich layer has been formed near the surface. This is likely due to the increased amount of extended defects at the GeSn/Ge interface due to the relaxation [32], as well as changes in the surface topography detected by AFM measurements. The dislocation fingerprints are seen clearly in AFM images (see Fig. 3) as the crosshatch patterns at the GeSn surface, becoming more pronounced as the film thickness increases, while the surface rms roughness increases linearly.

Figure 6 shows the evolution of the PC spectra for samples S45 and S200 in the temperature range 10–200 K. The observed step in the PC spectra near 0.8–0.85 eV corresponds to the direct band gap of the Ge buffer, which shifts by 38 meV towards higher energies as the temperature decreases 200–10 K following the Varshni relation as expected [33]. Otherwise, the low-energy edge of the low-temperature PC spectra, which is related to the GeSn absorption edge, is seen to shift to higher energies when heating. Figure 7(a) shows the near-band-gap spectra plotted in the Tauc equation coordinates, while Fig. 7(b) summarizes these results for the resulting temperature dependence of the direct band gap for samples S45 (strained) and S200 (partially relaxed) in the temperature range 10–150 K. The position of the PC edge increases linearly with the temperature with a linear coefficient of 0.43 meV K^{-1} for fully strained and 0.08 meV K^{-1}

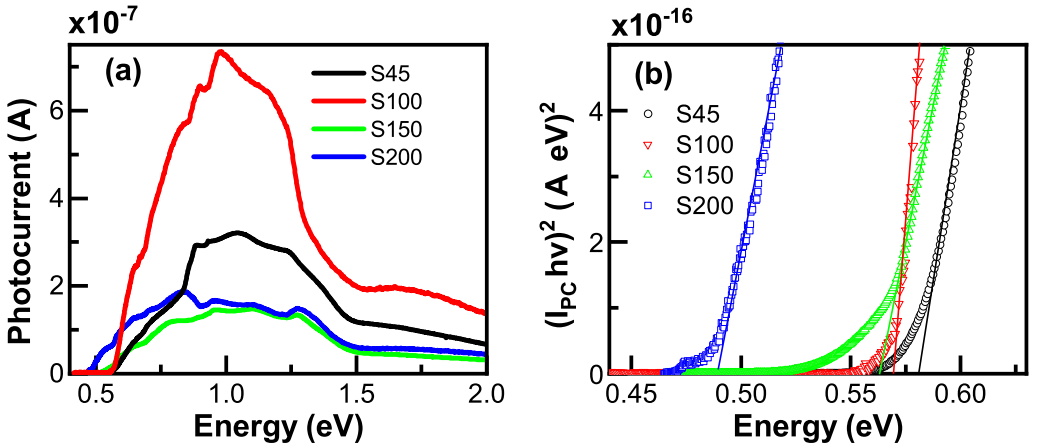

FIG. 5. The lateral PC spectra of the GeSn/Ge/Si heterostructures at 10 K (a) and their near-edge region in the Tauc coordinates $(I_{PC}hv)^2$ vs hv (b).

for the partially relaxed films in the temperature range 50–150 K.

The energies of near-band gap optical transitions obtained from PC measurements were compared with the position of the PL bands. Temperature-dependent PL spectra of samples S45 and S200 are shown in Fig. 8, for example. For all studied samples, two PL peaks related to the direct and indirect transitions can be identified at each temperature in the range of 10–200 K. These peaks have a small separation and a large spectral overlap due to the small separation of their respective energy levels for the strained GeSn alloys with Sn content around 12%. For the thicker sample, S200, the peaks are broader and redshifted in comparison with sample S45 at each temperature, confirming a higher Sn content accompanied by the associated strain relaxation.

C. Temperature dependence of the photoconductivity

Besides shifting to higher energies with temperature, the PC spectra demonstrated differing contributions from the GeSn, the Ge buffer, and the Si substrate depending on the temperature. In particular, the GeSn-related PC decreases with temperature increase more rapidly than that from Ge and Si, disappearing at temperatures above 200 K, while the contribution from the Ge buffer and the Si substrate decreased only moderately. To illustrate these changes, Fig. 9 presents the plots of the photocurrent vs $1/T$ (PCT) from 10 to 200 K measured under excitation energies of 0.6, 1.0, 1.33, and 1.5 eV. The lowest energy value of 0.6 eV was selected to absorb only into the GeSn films, while the Ge buffer and Si substrate are transparent. At this excitation energy, the photocurrent shows a few-order monotonous decrease when increasing the temperature, allowing us to find the activation energies from the slope of the linear parts of the Arrhenius plot of $\ln(I_{PC})$ vs $(k_BT)^{-1}$. From 130 to 170 K (see Fig. 5S in the Supplemental Material [28]) the activation energy is 78 meV and from 176 to 193 K the activation energy is 237 meV for sample S45.

At the same time, the slope of the linear sections of the Arrhenius plot of $\ln(I_{PC})$ vs $1/kT$ in the temperature range from 110 to 163 K (see Supplemental Material, Fig. 5S [28]) gives 23 meV, while from 173 to 232 K it gives 39.5 meV for the activation energies of sample S45 when analyzing the PCT curves under the predominant excitation in the Ge buffer layer together with the GeSn layer by 1.0 eV photons. These activation energies have not been observed under 0.6 eV excitation when only the GeSn layer was excited. This is generally due to the Ge buffer contributing the dominant photocurrent that is nearly two orders higher than that from GeSn using 1.0 eV excitation at high temperatures. Further increase of

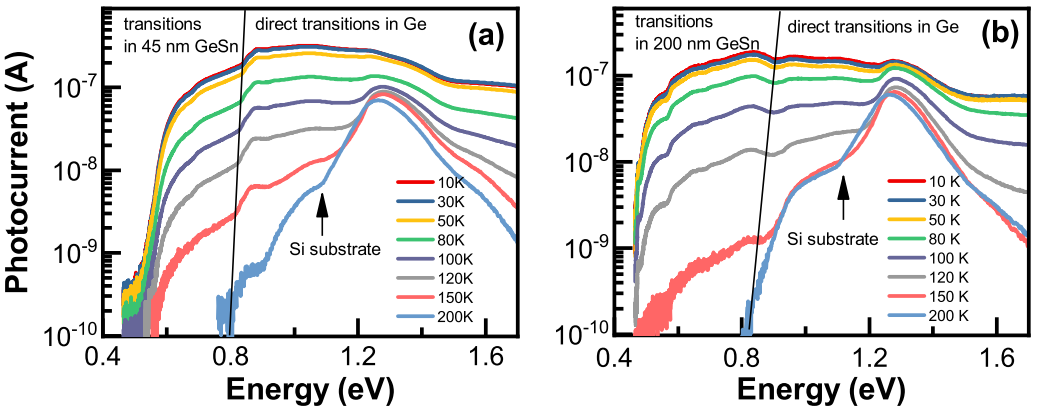

FIG. 6. The PC spectral dependencies for S45 (a) and S200 (b) samples measured at various temperatures in the range of 10–200 K.

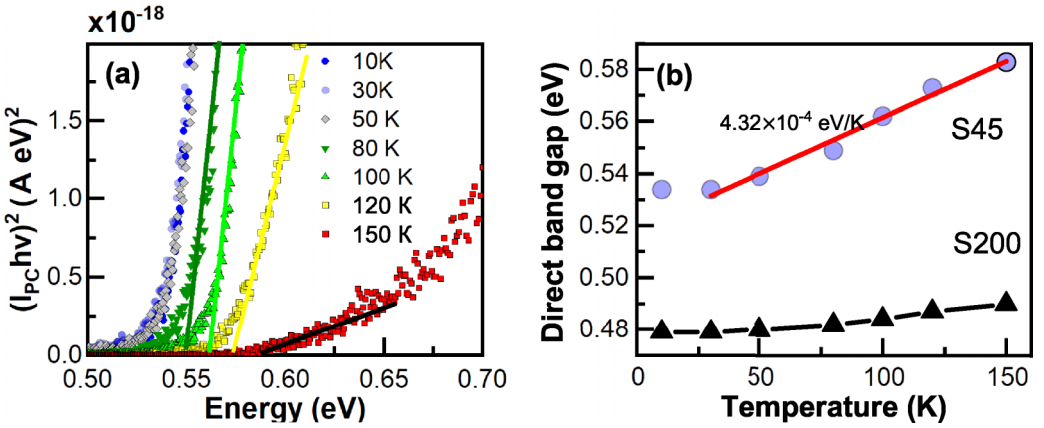

FIG. 7. The edges of the PC spectra of Fig. 6(a) in the Tauc coordinates (a) and the resulting temperature dependence of direct-band-gap for samples S45 and S200 in the temperature range 10–150 K (b).

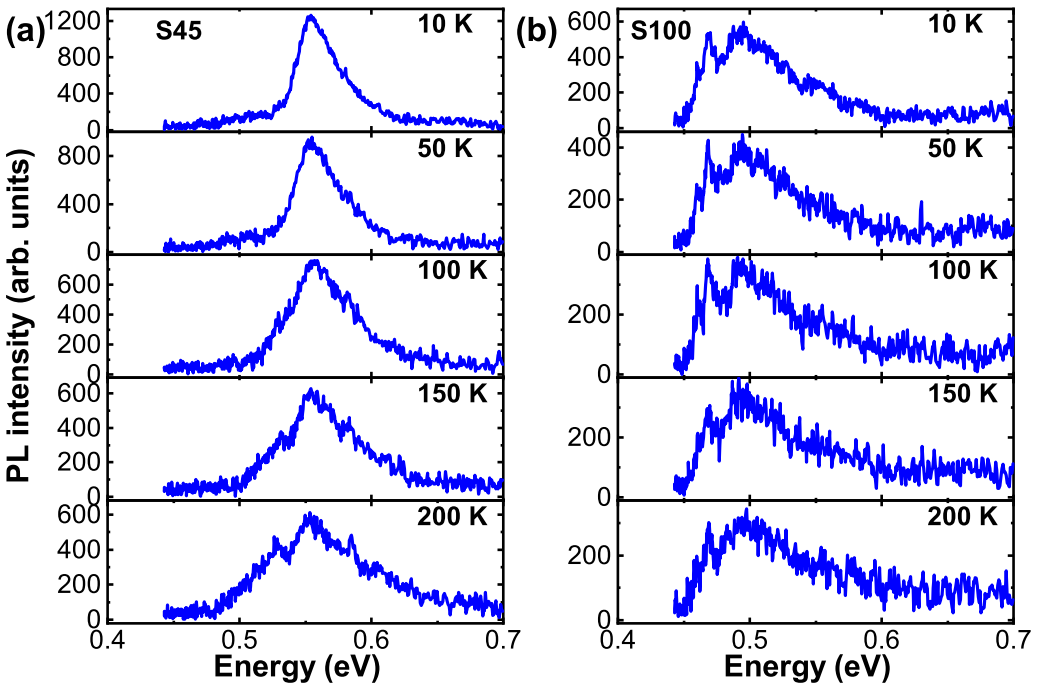

FIG. 8. The PL spectral dependencies for S45 (a) and S200 (b) samples measured at various temperatures in the range of 10–200 K.

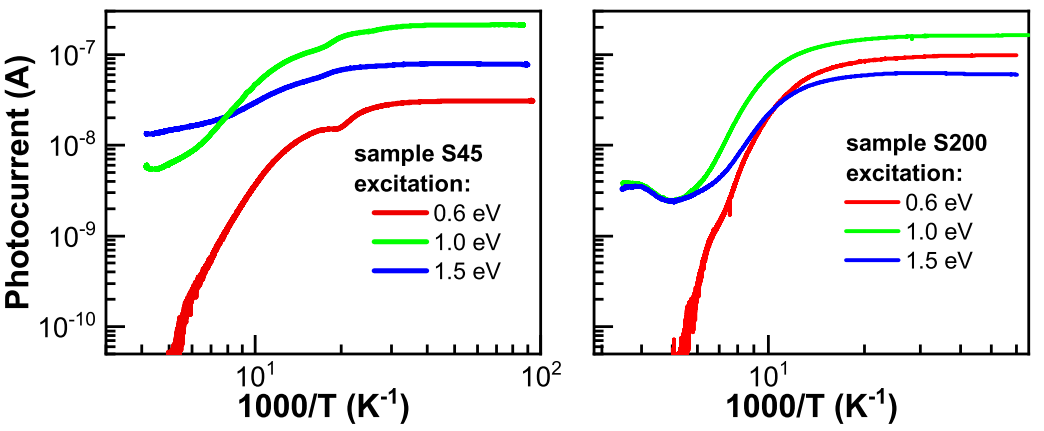

FIG. 9. The temperature dependence of PC for samples S45 (left) and S200 (right) at various excitation energies.

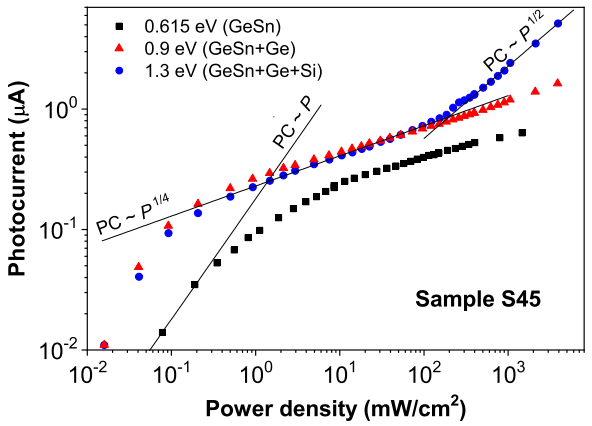

FIG. 10. PC vs excitation intensity at different excitations corresponding to edge absorption of the respective layers in sample S45 at 80 K.

the excitation energy to 1.5 eV allows generation of charge carriers in the GeSn, Ge, and Si layers simultaneously. The penetration of the light to the Si substrate (at least a few percent of the incidence light) together with higher absorbance by top layers leads to observing other activation energies of 10 and 15 meV that may be assigned to GeSn. It suggests that the Ge buffer and GeSn film are the predominant conductive paths for the carriers photoexcited both in Ge and GeSn, whereas the GeSn film contributes more to equivalent conductivity and photoconductivity as the temperature decreases.

D. Intensity dependence of photoconductivity

The spectral distribution of the photocurrent depends on the excitation intensity, because the photoresponse is not linear with the power density, P, for all energies. However, the dependence of the photocurrent on power density is quite similar for all the studied structures, so Fig. 10 presents such a plot for sample S45 as an example.

The photocurrent is linear with the excitation power for all energies in the low intensities range, up to ~ 0.2 mW/cm^2. Above this, all excitation energies demonstrate sublinear dependences with increased pumping power, which generally remains up to the highest powers. This dependence is typical for doped semiconductors and can be explained by simple calculations. Let the semiconductor have no impurities except for dopants, which are assumed to have a negligible effect on the optical excitation and recombination kinetics. In this case, the kinetic equation for the charge-carrier concentrations under band-to-band excitation is

$$\partial n/\partial t \;=\; \partial p/\partial t \;=\; g - \gamma(np - n_0 p_0), \tag{3}$$

where $g \propto P$ is the optical generation rate of the carrier pairs, and γ is a bimolecular recombination coefficient. The electron and hole concentrations are given by $n = n_0 + \Delta n$ and $p = p_0 + \Delta p$, where n_0 and p_0 are the equilibrium density of electrons and holes originating from thermal excitation from either the deep levels or the valence band, and Δn and Δp are the respective densities of the photogenerated carriers. Finally, we have

$$\begin{aligned}\partial(\Delta n)/\partial t &= \partial(\Delta p)/\partial t \\ &= g - \gamma(n_0\Delta p \;+\; p_0\Delta n + \Delta n\Delta p).\end{aligned} \tag{4}$$

We can then consider two extreme cases.

Case 1: The population of the photoexcited carriers is low; i.e., $\Delta n\Delta p \ll n_0\Delta p + p_0\Delta n$ (low excitation).

In a p-type semiconductor,

$$\partial(\Delta n)/\partial t = \partial(\Delta p)/\partial t = g - \gamma n_0 \Delta p. \tag{5}$$

Under the stationary excitation, $\partial(\Delta p)/\partial t = 0$, the stationary or steady state ($t \to \infty$) concentration of the nonequilibrium carriers becomes

$$\Delta p = (\Delta p)_\infty = g/(\gamma n_0), \tag{6}$$

or, considering $g \propto P$, we have a linear dependence of the nonequilibrium concentration (photoconductivity) on excitation intensity:

$$\Delta p \sim P. \tag{7}$$

Case 2: The nonequilibrium concentrations are high; i.e., $\Delta n\Delta p = (\Delta n)^2 \gg n_0\Delta p + p_0\Delta n$ (high excitation).

In this case,

$$\partial(\Delta n)/\partial t = g - \gamma\,\Delta n\Delta p = g - \gamma(\Delta n)^2. \tag{8}$$

Respectively, under the stationary excitation

$$\Delta n_\infty \sim (g/\gamma)^{1/2}, \tag{9}$$

or

$$\Delta p \sim P^{1/2}. \tag{10}$$

Therefore, we should observe linear dependence under low excitation and square root dependence for higher intensities. It should be noted that the experimental data follow this model strictly only for an excitation energy of 1.3 eV, where the light is high enough energy to be absorbed by the thick silicon substrate.

However, a $\frac{1}{4}$ power law dependence, $\sim P^{1/4}$, is also observed, indicating the existence of parallel conductivity channels for photoexcited charge carriers. In particular, this becomes dominant under higher excitations at energies below 1 eV when only the GeSn layer and Ge substrate are excited. Such a function is characteristic for layered structures under band-to-band excitation, where the nonequilibrium carriers excited in the predominant conductivity channel are supplemented by ones generated in neighboring layers [34]. As this kind of dependence is observed under 0.6 eV, when the Ge layer does not absorb, we believe that just the Ge layer is the predominant conductivity channel in our structures rather than the more conductive but much thinner GeSn top layer. However, a transformation of this dependence into the square root one under higher intensities for 1.3 eV excitation indicates that the thick Si substrate becomes the predominant conductivity channel for very high energy excitation, as it absorbs most of the incident light.

IV. DISCUSSION

By studying the photoconductivity at different temperatures, excitation wavelengths, and intensities, we have

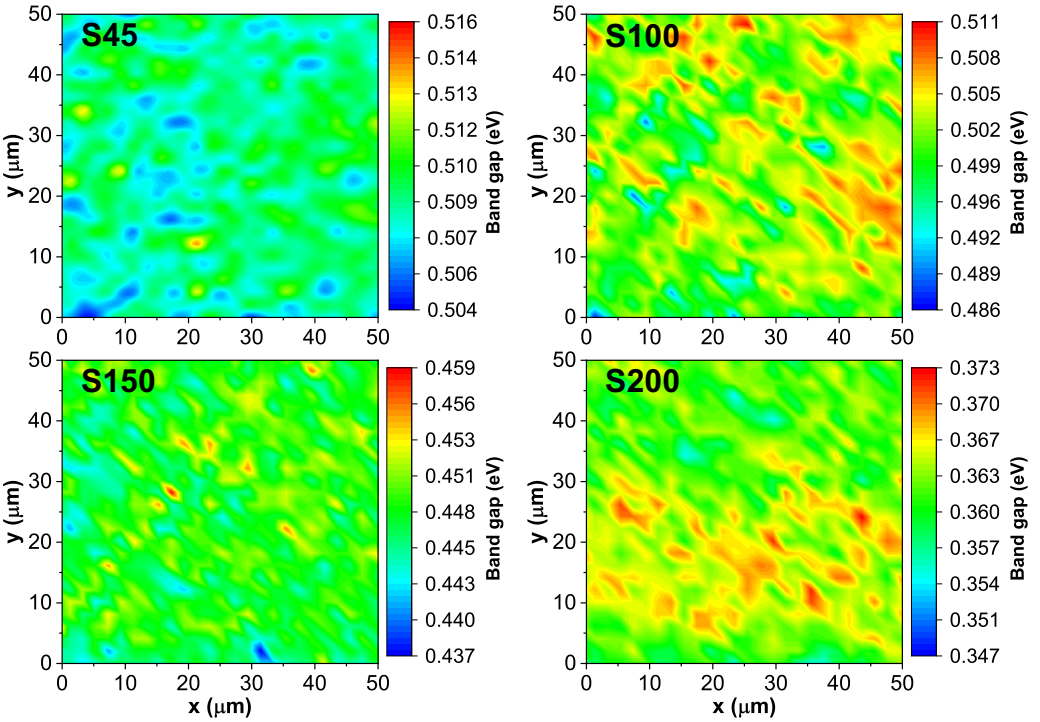

FIG. 11. Calculated band gap maps for samples of various thicknesses.

gathered direct insights into the impact of strain fields and/or strain-induced defect states on photoconductivity, as well as the transport path for the photoexcited charge carriers and the recombination activity of strain-induced defects in these GeSn/Ge/Si heterostructures. It was shown that strain and the resulting plastic relaxation significantly affected the GeSn-related IR photoresponse and decreased the Ge buffer and Si substrate contributions of the thicker strain-relaxed samples (S150 and S200) despite their higher absorptivity. As follows from Raman and XRD measurements, these samples demonstrate an increased Sn content (13.7% for S150 and 14.9% for S200) in their near-surface layers even though the Sn content in the bottom layer was generally the same (about 12%) for all studied samples. In turn, the formation of a Sn-enriched upper surface layer with a smaller band gap draws charge carriers towards the illuminated surface, increasing the surface recombination rate. Such an effect is well known for semiconductors with a graded band gap, where the flow of the minor charge carriers generally follows the lower band gap material. In this case, the contribution of surface recombination is enhanced compared to the rate of recombination in the bulk, which leads to a decrease in photosensitivity over a wide spectral range.

In addition to the Sn content changing across the thick GeSn film, lateral variations in the local Sn content and strain values may also improve an IR photoresponse. In particular, these lateral variations lead to in-plane variations in the absorber band edges in the near-surface region of the GeSn films. The maps and histograms of band gaps were calculated to characterize quantitatively the differences between samples of various thicknesses using the approach described in detail in Ref. [21] taking into account the strain and Sn content derived from the Raman measurements. Figure 11 shows these maps, illustrating the lateral variation of the direct band gap. This is considered within a few tens of nanometers from the surface due to the penetration depth of the Raman excitation laser.

It is well known that local quasielectric fields in graded-gap semiconductors originate from the conduction band and valence band variations with the position [35,36]. These internal fields may cause the observed shifts of the PC edges towards lower energies with decreasing T in contrast to most compound semiconductors where the band gap increases follows the Varshni equation [33]. A similar response has been observed in the low-temperature region of the optical spectra for Cu_2SnS_3 [37], Ag $Ga_{1-x}In_xSe_2$ [38], and Cu_2InS_3 compounds [39]. For our samples, as the band gap changes across the surface, we create localized wells for equilibrium (thermally generated) carriers to sit. This turns off the absorption into these lower-energy wells and thus pushes the apparent PC edge to higher energies. As the temperature decreases, the equilibrium carriers vanish leaving the lower-energy wells available for absorption, thus shifting the band edge to lower energy with decreasing temperature. The highest shift of 0.43 meV K^{-1} was observed in the temperature range 50–150 K for the fully strained film (S45), while it was 0.08 meV K^{-1} for S200, where strain relaxation has lowered the impact on band gap variation resulting from the same composition variations. It should be noted that the low-energy side of the PL peak (see Fig. 8) shifts to lower energy (redshift) with increasing temperature, which is opposite the trends of the PC edges. This means that temperature-induced changes in the position of PC spectral edges are not the result of the temperature dependence of the GeSn band gap, but are the result of the low-energy states being increasingly filled with increasing temperature. Thus, as they fill, the absorption edge shifts to higher energy with increasing temperature. The effect

becomes increasingly pronounced as the concentration of the intrinsic charge carriers increases with temperature.

As the temperature increases, when kT becomes higher than the in-plane band gap variations (5–10 meV), spatial separation becomes less effective and, therefore, the GeSn-related PC decreases by a few orders. This is the direct result of SRH recombination centers in the GeSn bulk or GeSn/Ge interface. Considering the linear parts of the Arrhenius plot of the photocurrent with 0.6 eV excitation in the high-temperature range [see Fig. 9(a)], one can explain the temperature dependence of the PC qualitatively, assuming the presence of shallow acceptor states responsible for the p-type conductivity of the GeSn films. At high temperatures, all of the acceptors are ionized, creating free holes in the valence band. In this case, the SRH recombination reduces the concentration of minority charge carriers, i.e., electrons, whose equilibrium concentration is determined by the efficiency of band-to-band free carrier generation and given by

$$n_i = \sqrt{N_c N_v}\exp\left(-\frac{\varepsilon_g}{2k_B T}\right), \tag{11}$$

where N_c and N_v are the effective density of states in the conduction and valance bands, respectively; ε_g is the band gap; k_B is Boltzmann's constant; and T is temperature. As a result, the linear part with the highest slope gives $\varepsilon_g/2 = 237$ meV or $\varepsilon_g = 474$ meV under 0.6 eV excitation for sample S45 (see Supplemental Material, Fig. 5S [28]). This agrees with the direct–band-gap value derived from the analysis of the PC spectra. The second activation energy of 78 meV derived from the PCT curve at 0.6 eV excitation corresponds to the misfit dislocation levels in GeSn. Earlier, we showed that these acceptorlike states are positioned at ∼ 85–90 meV above the valence band maximum and act as SRH centers determining the charge-carrier lifetime for alloys of lower Sn content of about 1%–4% [18]. In general, the generation of point defects is more probable as the Sn content decreases. This, together with the increased intrinsic charge-carrier concentration resulting from heating the narrow-gap GeSn alloys, should lead to more efficient SRH channels. The observed quenching of the GeSn-related PC at temperatures above 150 K in all studied samples can then be attributed also to the simultaneous impact of surface and interface recombination during long-distance drift of the photoexcited charge carriers in the thin GeSn layers.

At the same time, the PC components related to the Ge buffer, observed with 1.0 eV excitation, and the Si substrate, observed with 1.3 eV excitation, decrease less with increased temperature due to the impact of other kinds of recombination centers located in the Ge/Si virtual substrate. This is indicated by the different activation energies from PCT analysis. In addition, their relative contribution to the photoconductivity spectra increased with temperature against the contribution of the quickly disappearing GeSn component. This means that the Ge buffer and the Si substrate, as well as the Ge/Si interface, are the predominant transport paths for the photoexcited charge carriers at high temperatures despite the presence of a more conductive but much thinner GeSn top layer. The validity of this assumption is confirmed by the spectral dependences of the photoconductivity (see Fig. 6), where the contributions originating from light absorption by the Ge buffer significantly exceed that from the GeSn. In addition, at temperatures above 200 K, this component was observed in the PC spectra only with the contribution from the Si substrate, whereas the contribution from GeSn was not detected. Meanwhile, the transport of photoexcited charge carriers through the neighboring GeSn becomes more significant at low temperatures due to the reduced probability of SRH recombination, the lower position of the conduction band, and the higher position of the valence band compared to the Ge buffer.

V. CONCLUSIONS

Photoconductivity at different temperatures, excitation wavelengths, and intensities clarifies a mechanism of the photoexcited charge-carrier recombination and transport along GeSn/Ge/Si heterostructures. Our study emphasizes the crucial role of variations of both the Sn content and the strain in GeSn films with higher Sn content. It was shown that GeSn-related photoconductivity near the GeSn band gap decreases when strain release occurs due to the generation of misfit dislocations at the GeSn/Ge interface as the thickness of the GeSn layer increases. Besides the impact on the GeSn-related infrared photoresponse, strain fields lead to an anomalous blueshift of the band edge in PC spectra, namely, it linearly increases as the lattice temperature increases from 10 to 200 K with a linear coefficient of 0.43 meV K^{-1} for fully strained and 0.08 meV K^{-1} for partially relaxed films. The in-plane variations of the Sn content and strain in the GeSn films of high Sn content are responsible for the observed shift of the PC spectra originating from a variation of the band gap energies and increased contribution to the PC from the region of highest Sn content. By analyzing the evolution of the PC spectra with temperature and photon energies for a set of samples of various thicknesses and strains, we have found that the transport paths of photoexcited charge carriers occur mainly through the Ge buffer at high temperatures. At the same time, the GeSn film contributes more in parallel to equivalent conductivity and photoconductivity as temperature decreases. Furthermore, the photocurrent dependencies on excitation intensity demonstrate that the primary conduction occurs mainly through the GeSn and Ge layers under low excitation intensity and through the Si substrate under high excitation intensity since the GeSn top layer is much thinner and has a much higher conductivity. This detailed understanding of the transport of photoexcited carriers along the GeSn layers is critical for developing GeSn/Ge-based optoelectronic devices.

ACKNOWLEDGMENTS

This publication is based on work supported by a Multidisciplinary University Research Initiative (MURI) Program through the U.S. Air Force Office of Scientific Research (AFOSR) Grant No. FA9550-19-1-0341 and the National Research Foundation of Ukraine (Grant No. 2020.02/0134).

The authors declare no competing financial interest.

[1] Y. Miao, G. Wang, Z. Kong, B. Xu, X. Zhao, X. Luo, H. Lin, Y. Dong, B. Lu, L. Dong *et al.*, Review of Si-based GeSn CVD growth and optoelectronic applications, Nanomaterials **11**, 2556 (2021).

[2] A. Nadtochiy, V. Kuryliuk, V. Strelchuk, O. Korotchenkov, P.-W. Li, and S.-W. Lee, Enhancing the Seebeck effect in Ge/Si through the combination of interfacial design features, Sci. Rep. **9**, 16335 (2019).

[3] K. L. Low, Y. Yang, G. Han, W. Fan, and Y.-C. Yeo, Electronic band structure and effective mass parameters of $Ge_{1-x}Sn_x$ alloys, J. Appl. Phys. **112**, 103715 (2012).

[4] C. Eckhardt, K. Hummer, and G. Kresse, Indirect-to-direct gap transition in strained and unstrained Sn_xGe_{1-x} alloys, Phys. Rev. B **89**, 165201 (2014).

[5] S. Wirths, V. Reboud, A. Gassenq, N. Pauc, J. Aubin, L. Milord, Q. M. Thai, M. Bertrand, K. Guilloy, D. Rouchon *et al.*, Lasing in direct-bandgap GeSn alloy grown on Si, Nat. Photonics **9**, 88 (2015).

[6] Y. Zhou, W. Dou, W. Du, S. Ojo, H. Tran, S. A. Ghetmiri, J. Liu, G. Sun, R. Soref, J. Margetis *et al.*, Optically pumped GeSn lasers operating at 270 K with broad waveguide structures on Si, ACS Photonics **6**, 1434 (2019).

[7] S. Ghosh, K.-C. Lin, C.-H. Tsai, H. Kumar, Q. Chen, L. Zhang, B. Son, C. S. Tan, M. Kim, B. Mukhopadhyay *et al.*, Metal-Semiconductor-metal GeSn photodetectors on silicon for short-wave infrared applications, Micromachines **11**, 795 (2020).

[8] H. H. Tseng, H. Li, V. Mashanov, Y. J. Yang, H. H. Cheng, G. E. Chang, R. A. Soref, and G. Sun, GeSn-based $p-i-n$ photodiodes with strained active layer on a Si wafer, Appl. Phys. Lett. **103**, 231907 (2013).

[9] H. Wang, S. Masudy-Panah, S. Xu, W. Wang, X. Gong, Y.-C. Yeo, Y.-C. Huang, and Y. Dong, High-speed photo detection at two-micron-wavelength: Technology enablement by GeSn/Ge multiple-quantum-well photodiode on 300 mm Si substrate, Opt. Express **27**, 5798 (2019).

[10] W. Wang, D. Lei, Y.-C. Huang, K. H. Lee, W.-K. Loke, Y. Dong, S. Xu, C. S. Tan, H. Wang, S.-F. Yoon *et al.*, High-performance GeSn photodetector and fin field-effect transistor (FinFET) on an advanced GeSn-on-insulator platform, Opt. Express **26**, 10305 (2018).

[11] R. W. Olesinski and G. J. Abbaschian, The Ge–Sn (germanium–tin) system, Bull. Alloy Phase Diagrams **5**, 265 (1984).

[12] L. Zhang, Y. Song, N. von den Driesch, Z. Zhang, D. Buca, D. Grützmacher, and S. Wang, Structural property study for GeSn thin films, Materials **13**, 3645 (2020).

[13] H. V. Stanchu, A. V. Kuchuk, Y. I. Mazur, J. Margetis, J. Tolle, S.-Q. Yu, and G. J. Salamo, Strain suppressed Sn incorporation in GeSn epitaxially grown on Ge/Si(001) substrate, Appl. Phys. Lett. **116**, 232101 (2020).

[14] C. M. Comrie, C. B. Mtshali, P. T. Sechogela, N. M. Santos, K. van Stiphout, R. Loo, W. Vandervorst, and A. Vantomme, Interplay between relaxation and Sn segregation during thermal annealing of GeSn strained layers, J. Appl. Phys. **120**, 145303 (2016).

[15] F. Gencarelli, Y. Shimura, A. Kumar, B. Vincent, A. Moussa, D. Vanhaeren, O. Richard, H. Bender, W. Vandervorst, M. Caymax *et al.*, Amorphous inclusions during Ge and GeSn epitaxial growth via chemical vapor deposition, Thin. Solid. Films **590**, 163 (2015).

[16] M. Coppinger, J. Hart, N. Bhargava, S. Kim, and J. Kolodzey, Photoconductivity of germanium tin alloys grown by molecular beam epitaxy, Appl. Phys. Lett. **102**, 141101 (2013).

[17] J. Hart, T. Adam, Y. Kim, Y.-C. Huang, A. Reznicek, R. Hazbun, J. Gupta, and J. Kolodzey, Temperature varying photoconductivity of GeSn alloys grown by chemical vapor deposition with Sn concentrations from 4% to 11%, J. Appl. Phys **119**, 93105 (2016).

[18] S. Kondratenko, S. Derenko, Y. I. Mazur, H. Stanchu, A. V. Kuchuk, V. S. Lysenko, P. Lytvyn, S.-Q. Yu, and G. J. Salamo, Impact of defects on photoexcited carrier relaxation dynamics in GeSn thin films, J. Phys.: Condens. Matter **33**, 065702 (2020).

[19] B. Son, L. Zhang, Y. Jung, H. Zhou, D. Nam, and C. S. Tan, Systematic study on photoexcited carrier dynamics related to defects in GeSn films with low Sn content at room temperature, Semicond. Sci. Technol. **36**, 125018 (2021).

[20] H. Tran, C. G. Littlejohns, D. J. Thomson, T. Pham, A. Ghetmiri, A. Mosleh, J. Margetis, J. Tolle, G. Z. Mashanovich, W. Du *et al.*, Study of GeSn mid-infrared photodetectors for high frequency applications, Front. Mater. **6**, 00278 (2019).

[21] S. V. Kondratenko, Y. V. Hyrka, Y. I. Mazur, A. V. Kuchuk, W. Dou, H. Tran, J. Margetis, J. Tolle, S. Q. Yu, and G. J. Salamo, Photovoltage spectroscopy of direct and indirect bandgaps of strained $Ge_{1-x}Sn_x$ thin films on a Ge/Si(001) substrate, Acta Mater. **171**, 40 (2019).

[22] J. Margetis, S.-Q. Yu, B. Li, and J. Tolle, Chemistry and kinetics governing hydride/chloride chemical vapor deposition of epitaxial $Ge_{1-x}Sn_x$, J. Vac. Sci. Technol., A **37**, 021508 (2019).

[23] D. J. Lockwood and Z. R. Wasilewski, Optical phonons in $Al_xGa_{1-x}As$: Raman spectroscopy, Phys. Rev. B **70**, 155202 (2004).

[24] Bouthillier, S. Assali, J. Nicolas, and O. Moutanabbir, Decoupling the effects of composition and strain on the vibrational modes of GeSn semiconductors, Semicond. Sci. Technol. **35**, 095006 (2020).

[25] V. R. D'Costa, J. Tolle, R. Roucka, C. D. Poweleit, J. Kouvetakis, and J. Menéndez, Raman scattering in $Ge_{1-y}Sn_y$ alloys, Solid State Commun. **144**, 240 (2007).

[26] J.-H. Fournier-Lupien, S. Mukherjee, S. Wirths, E. Pippel, N. Hayazawa, G. Mussler, J. M. Hartmann, P. Desjardins, D. Buca, and O. Moutanabbir, Strain and composition effects on Raman vibrational modes of silicon-germanium-tin ternary alloys, Appl. Phys. Lett. **103**, 263103 (2013).

[27] E. A. Fitzgerald, Y.-H. Xie, D. Monroe, P. J. Silverman, J. M. Kuo, A. R. Kortan, F. A. Thiel, and B. E. Weir, Relaxed Ge_xSi_{1-x} structures for III–V integration with Si and high mobility two-dimensional electron gases in Si, J. Vac. Sci. Technol., B: Microelectron. Nanometer Struct.–Process., Meas., Phenom. **10**, 1807 (1998).

[28] See Supplemental Material at http://link.aps.org/supplemental/10.1103/PhysRevMaterials.7.074604 for the maps and histograms for Sn content and strain for the GeSn samples derived from the measured Raman spectra; the temperature dependence of photoconductivity at excitations 0.6, 1.0, and 1.5 eV at 10 K.

[29] C. Xu, C. L. Senaratne, R. J. Culbertson, J. Kouvetakis, and J. Menéndez, Deviations from Vegard's law in semiconductor thin films measured with x-ray diffraction and Rutherford backscattering: The $Ge_{1-y}Sn_y$ and $Ge_{1-x}Si_x$ cases, J. Appl. Phys. **122**, 125702 (2017).

[30] D. Stange, S. Wirths, N. von Den Driesch, G. Mussler, T. Stoica, Z. Ikonic, J. M. Hartmann, S. Mantl, D. Grützmacher, and D. Buca, Optical transitions in direct-bandgap $Ge_{1-x}Sn_x$ alloys, ACS Photonics **2**, 1539 (2015).

[31] V. R. D'Costa, W. Wang, Q. Zhou, and E. Soon Tok, and Y. C. Yeo, Above-bandgap optical properties of biaxially strained GeSn alloys grown by molecular beam epitaxy, Appl. Phys. Lett. **104**, 022111 (2014).

[32] F. Pezzoli, A. Giorgioni, D. Patchett, and M. Myronov, Temperature-dependent photoluminescence characteristics of GeSn epitaxial layers, ACS Photonics **3**, 2004 (2016).

[33] Y. P. Varshni, Temperature dependence of the energy gap in semiconductors, Physica (Amsterdam) **34**, 149 (1967).

[34] S. L. Golovynskyi, O. I. Dacenko, S. V. Kondratenko, S. R. Lavoryk, Y. I. Mazur, Z. M. Wang, M. E. Ware, G. G. Tarasov, and G. J. Salamo, Intensity-dependent nonlinearity of the lateral photoconductivity in InGaAs/GaAs dot-chain structures, J. Appl. Phys. **119**, 184303 (2016).

[35] B. S. Sokolovskii, V. K. Pysarevskii, O. V. Nemolovskii, and Z. Swiatek, Theoretical study of the photovoltaic effect in thin variable-gap semiconductor layers, Thin Solid Films **431**, 457 (2003).

[36] S. V. Kondratenko, O. V. Vakulenko, Y. I. Mazur, V. G. Dorogan, E. Marega, M. Benamara, M. E. Ware, and G. J. Salamo, Deep level centers and their role in photoconductivity transients of InGaAs/GaAs quantum dot chains, J. Appl. Phys. **116**, 193707 (2014).

[37] N. Aihara, H. Araki, and K. Tanaka, Excitonic and band-to-band transitions in temperature-dependent optical absorption spectra of Cu_2SnS_3 thin films, Phys. Status Solidi **255**, 1700304 (2018).

[38] S.-R. Hahn and W.-T. Kim, Anomalous composition and temperature dependence of the energy gap of Ag $Ga_{1-x}In_xSe_2$ mixed crystals, Phys. Rev. B **27**, 5129 (1983).

[39] T. M. Hsu and J. H. Lin, Anomalous temperature-dependent band gaps in $CuInS_2$ studied by surface-barrier electroreflectance, Phys. Rev. B **37**, 4106 (1988).